Processing Bulk Nanostructured Materials

On the optimisation of phase fractions in harmonic structure materials

Abdallah Shokry[1], Per Ståhle[2], and Dmytro Orlov[3,*]

[1] *Mechanical Engineering, Faculty of Engineering, Fayoum University, Fayoum, Egypt*

[2] *Solid Mechanics, Lund University, Lund, Sweden*

[3] *Mechanics, Materials and Component Design, Lund University, Lund, Sweden*

ABSTRACT

Materials with heterogeneous microstructures architected across several scales are becoming increasingly popular in structural applications due to unique strength–ductility balance. One of the most popular 3D-architected structure designs is harmonic structure (HS) where soft coarse-grain (CG) islands are embedded in a hard continuous 3D skeleton of ultrafine grains (UFGs). In this work, a series of HS with varying phase fractions and rheologies are studied based on several models. Model A focuses on a good fit with experimental data in the elastic–plastic transition region, model B focuses on a good fit at large-scale yielding, while in five intermediate models, phase rheology parameters are varied on a linear scale between the values for A and B. For each of the seven selected HS material models, structures with 19 different volumetric fractions of UFG were examined. It is found that the increase of UFG fraction leads to the monotonic increase of strength characteristics in HS material, while higher strain hardening rates in the phases lead to the enhancement of this effect. By contrast, the dependence of ductility characteristics on UFG fraction is non-monotonic having a local minimum at 30% UFG and a maximum at 60% UFG, while also significantly dependent on strain hardening in the phases. Namely, HS material with phases having significant strain hardening reveals the highest uniform elongation exceeding that in 100% CG material already at 40% UFG fraction. The fractions of UFG in a range of 58–62% form HS material with the highest possible uniform elongation.

Introduction

The mechanical properties of metals and alloys are highly affected by grain size. It is well known that strength increases, and ductility decreases with decreasing grain sizes [1–3]. In the past few decades, ultrafine grain (UFG) structures have received much attention for their potential to give interesting mechanical and physical properties contrasting coarse-grain (CG) materials of similar compositions

---

🍂 Springer

[4, 5]. Despite significant achievements in preserving ductility in UFG materials, it is still often at a level significantly lower than desirable.

Fabricating a bimodal grain size distribution has been proposed to optimise the mechanical properties of metals for high strength and high ductility [6, 7]. Of particular interest in such an approach are harmonic structure (HS) materials in which the CG phase islands are surrounded by a three-dimensional skeletal network of the UFG phases [8–11]. The fabrication of HS materials is typically achieved by using powder metallurgy-based technology [10, 12]. Such a bimodal structure combines the ductility of CG and the strength of UFG for a multitude of metals [8, 9] including stainless steel [13, 14], titanium [15–17] and nickel [18, 19].

Numerical simulations using finite element methods are by far the most frequently used to investigate the plastic deformation behaviour of metals and alloys [20–22]. Also, the strain distributions of severe plastic deformation processes during the fabrication of homogeneous UFG have been studied using finite element methods [23–25]. Recently, simulations of dislocation dynamics and 3D crystal plasticity modelling were used to support theoretical results on deformation mechanisms in HS materials, cf. [26, 27]. Another recent 2D finite element model to study the influence of topological arrangements in ultrafine and coarse grains on the mechanical behaviour of pure nickel was presented by Shokry et al. [28]. Common for these studies is that they highlight the advantages of using a mixed ultrafine- and coarse-grain topology.

However, a detailed understanding of CG/UFG fraction ratios on the behaviour of such structures is still missing, and more work in this area is urgently needed. In the present work, nineteen 2D finite element structural arrangements with different fractions of CG and UFG phases and for each, the seven different UFG-CG pairs of material models are studied. The CG inclusions are uniformly distributed inside a network of a UFG skeleton. The von Mises equivalent stresses and plastic strains are investigated at and close to the ultimate load for the studied models. In addition, normal stress components as well as shear components are also studied. Furthermore, characteristic patterns of the failure path for a few of the models are observed.

The overall aim of the present work is to study the effect of the phase volume fractions on the mechanical properties of the bimodal structures. Special attention is devoted to the optimal volumetric skeleton content and its dependence on the selected material properties as described in the sub-section 2.1.

Materials testing and properties

The computational models of material rheologies in the present work are based on our earlier investigations of HS nickel. In those studies, metal powder with an average particle diameter of 149.5 μm was prepared by plasma rotating electrode process from commercially pure nickel. The particles were processed by mechanical milling to form a gradient structure in each of them and finally, these were spark-plasma sintered to fabricate harmonic structure compacts. The properties were examined in tensile tests. Further details of the procedures can be found in Refs. [18, 19].

Material models

Both CG and UFG phases are modelled as isotropic elastic–plastic with a strain hardening based on experimental data for both pure CG and UFG nickel. The Cauchy stresses, also called true stresses, $\sigma_x, \sigma_y,$ and σ_{xy} and logarithmic strains $\epsilon_x, \epsilon_y, \epsilon_z,$ and ϵ_{xy} are used for numerical analyses. According to established practice, the strains are split into elastic and plastic parts, i.e.

$$\epsilon_x = \epsilon_x^e + \epsilon_x^p, \ \epsilon_y = \epsilon_y^e + \epsilon_y^p, \text{ etc.} \tag{1}$$

The elastic stress–strain relationship is Hooke's law for which the elastic modulus, E, is taken to be 207 GPa and Poisson's ratio, $v = 0.31$ for both phases, cf. [29].

The original material properties are obtained at low strain rates, and the material models are assumed to be strain rate non-sensitive. The plastic strains are given by von Mises yield criterion together with its associated flow rule. Input plastic data, i.e. true flow stress and plastic strain for both CG and UFG phases are fitted to the experimental data by using a Hollomon stress–strain relationship. The equivalent stress, σ, related to von Mises' yield criterion is approximated by power functions of the corresponding equivalent total strain, ϵ, as follows,

$$\sigma = k\epsilon^s, \tag{2}$$

where the coefficients k assume the values $k = k_{\text{UFG}}$ MPa and $k = k_{\text{CG}}$ MPa for the UFG and the CG, respectively. The corresponding powers $s = s_{\text{UFG}}$ and $s = s_{\text{CG}}$. Both k and s are determined from tensile testing.

The yield stress, σ_{Y}, can be calculated using Eqs. 1 and 2 and the fact that the plastic part of the effective strain $\epsilon^p = 0$ at the initiation of yielding, i.e. when $\sigma = \sigma_{\text{Y}}$. For uniaxial stress, the elastic strain $\epsilon = \sigma_{\text{Y}}/E$, which requires that,

$$k = E^s \sigma_{\text{Y}}^{1-s}. \tag{3}$$

Inserted in Eq. 2 it gives the following alternative form for the power law,

$$\sigma = \sigma_{\text{Y}}^{1-s}(E\epsilon)^s. \tag{4}$$

According to [18], the yield stress is $\sigma_{\text{Y,CG}} = 49.3$ MPa for CG and $\sigma_{\text{Y,UFG}} = 371$ MPa for UFG. Equation 3 imposes a restriction for the measured yield stress, σ_{Y}, and the fitted power law coefficient, k. The parameters k and s are fitted to approximate the plastic behaviour at large plastic straining while the measured yield stress σ_{Y} is obtained at vanishing plastic straining. The parameters σ_{Y} and k originate from different measurements, cf. [18]. Therefore, it is not surprising that the two values are slightly incompatible with Eq. 4.

The inclusions of the softer CG phase are assumed to be exposed to mild compression and shear, while the harder UFG phase skeleton is expected to carry a larger part of the tensile load [30, 31]. The attempt of the present paper is to explore what a significant change in material properties would lead to. Preliminary results were not significantly affected by the choice of governing Eq. 2 or its alternative 4. This and the paramount role of the skeleton and its strength motivated the use of a UFG phase that has a higher hardening rate.

The available mechanical testing of the UFG phase is limited to straining of only a couple of per cent due to early onset of plastic instability. The failure that includes fracture is not included in the present study. One of the reasons not to include fracture is that the hydrostatic stress, which triggers void growth and ductile fracture, is assumed to be low. The assumption is motivated by the very thin almost wirelike skeletal structure of the UFG material that, embedded as it is by softer CG material, does not develop high hydrostatic stresses. At the same time, it should be noted that low hydrostatic stresses do not guarantee the absence

of dilatancy, which can exist at low and even high hydrostatic pressures and be one of the reasons for premature material fracture. cf. [32].

As a consequence of the very small ultimate strain at the testing of the pure UFG material, the fitting of s and σ_{Y} to the test results is rather uncertain. Therefore a wider spectrum of UFG phase rheologies is included in the present study. An augmented UFG model A with a larger power law exponent s and a basic model B based on the measured exponents. The basic model B, phase pair is based on the hardening experimentally obtained, cf. [18], $s_{\text{UFG-B}} = 0.106$ for the UFG phase and $s_{\text{CG-B}} = 0.376$ for the CG phase, and the augmented model A where both materials are given the same exponents $s_{\text{UFG-A}} = s_{\text{CG-A}} = 0.376$.

What remains is to adjust measured but incompatible values of the measured yield stress σ_{Y} vis-à-vis the power law parameters k and s. Here, the coefficient k is selected to be calculated to fit the measured yield stress for the UFG-A, UFG-B and CG-B models according to Eq. 3. For CG-A, the yield stress is calculated using the measured k. The latter provided an opportunity to confirm the preliminary results giving insignificant changes caused by the selection to calculate the yield stress σ_{Y} or alternatively the power law coefficient k.

All parameters are summarised in Table 1, in which the values that are calculated from other measured quantities are marked with an asterisk. The remaining data originates from tensile testing, cf. [18, 29]. Although the calculated yield strength (indicated with *) appears low, it gives the best fit to the plastic behaviour that can be obtained using the Hollomon relationship Eq. 2 on the available stress–strain data, cf. [18]. We do know that the calculated yield stress is somewhat lower than expected from literature (approximately 70 MPa). The change in this value does not have any significant effect on the final results of our simulations, which have a focus on strain levels that are several orders of magnitude larger.

The HS phase rheology models A and B give significantly different results, which motivate that calculations are performed also for intermediate phase rheologies. Thus, a range of phase rheologies is given by parameters k, σ_{Y}, and s, that are linearly scaled to fill in the gap between HS models A and B. The scaling is based on a parameter q and is performed as follows,

Table 1 HS phase rheology models A and B with the coefficient k calculated for phase rheologies UFG-A, UFG-B and CG-B using Eq. 3, the given yield stresses σ_Y and powers, s

Material	Yield stress, σ_Y [MPa]	Coefficient, k [MPa]	Power, s [-]
UFG-A	371	4000*	0.376
CG-A	28.41*	805	0.376
UFG-B	371	726*	0.106
CG-B	49.3	1135*	0.376

For CG-A the yield stress is calculated using the inverse of Eq. 3 and the given parameters k and s. Calculated values are marked with *

$$p = p_A(1 - q) + p_B q, \text{ where } q = 0, 0.1, 0.25, 0.5, 0.75, 0.9, 1 \quad (5)$$

while p replaces k or s, and with p_A and p_B replacing the corresponding parameters for models A and B. The yield stress σ_Y is readily calculated using the inverse of Eq. 3. Obviously, the extreme values $q = 0$ and $q = 1$ refer to pure models A and B, respectively, and the remaining q's are the five intermediate models.

Figure 1a shows an overview and Fig. 1b a close-up of a range of elongations that are assumed to be sufficient for all seven material models used. All the values are considered to be relevant, which also applies to those for $q < 0.5$ in spite of the fact that these are unrealistically high being dominated by model A. The

latter are useful for simulation purposes and keeping track of possible trends. However, in real life, the material will fracture well before reaching these values if the hydrostatic pressure in the deformation zone is low or will be suppressed to lower strain hardening values through a change in deformation mechanisms if the hydrostatic pressure is sufficiently high, cf. [33]. It should be noted that elongation levels up to ℓ, meaning an average engineering strain of 100%, are not expected because of the onset of plastic instability due to several events that may be initiated by large strain or stress. Mechanical testing procedures usually leave us with a truncated stress–strain curve. It ends because of fracture, plastic collapse, a mix or something else. The only failure mechanism included in the present study is failure due to the reduction of the cross-sectional thickness in a narrow region transversing the entire specimen typically called necking.

As observed the changes due to the choice between relying on the measured k and σ_Y as for the CG phase, are only minor. This is in contrast to the same including also a change of the power law exponent s makes larger changes as observed for the UFG phases. It may also be noted that the strength of the UFG phases ends up as lower than the strength of the CG phases for large elongations (see Figure 1b) for materials with $q \gtrsim 0.95$.
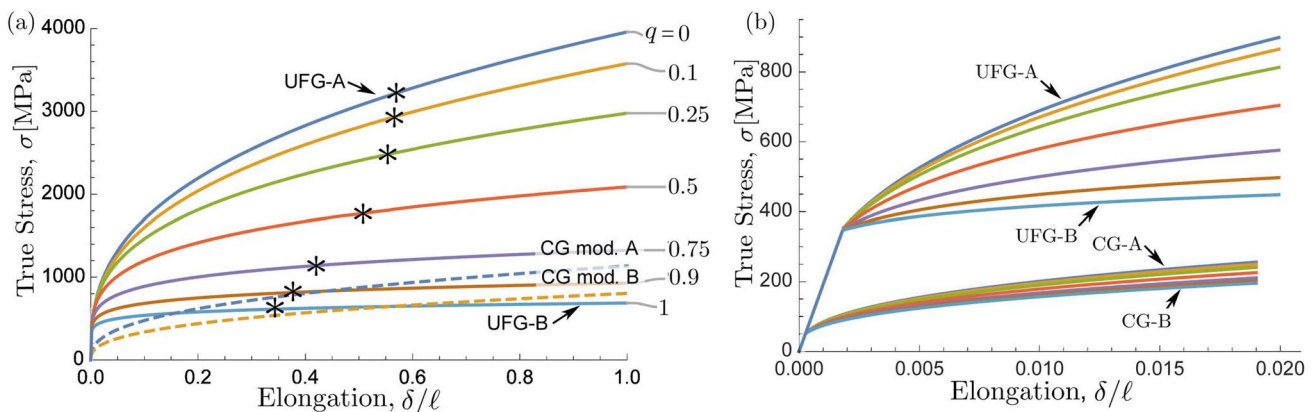

Figure 1 True stress versus normalised elongation δ/ℓ relationships for pure UFG and CG phases. The two models A and B and their intermediate models are given by the scaling parameter $q = 0, 0.1, 0.25, 0.5, 0.75, 0.90$ and 1, cf. Equation 5a shows the curves for an excessively large range of elongations. The maximum elongation reached in the model UFG phases before the beginning of global instability is marked with an asterisk. With full appreciation of excessively large values of strength a low $q < 0.5$ values, they are kept in the diagram for the visualisation of potential trends. For clarity, only the pure models A and B, i.e. $q = 0$ and 1 are included as dashed curves for CG. **b** shows the relations for elongation, δ/ℓ, up to 0.02 including the elastic part for which all models coincide.

Numerical modelling

The FE model in the present study corresponds to a quarter of the gage section of the tensile specimen with the harmonic structure, used in our earlier experimental work [14]. The prepared tensile sample dimensions had in the gage section length, height and thickness of $5 \times 1 \times 1$ mm^3. With the CG in-plane circular inclusions and UFG as a skeleton, the 2D model inclusions form a homogeneously close-packed structure. In the x–y plane, the 2D model is composed of periodic cells with dimensions of $\ell \times \ell$, where $\ell = 0.1$ mm. With 50 cells in the x-direction and 10 cells in the transverse y-direction, this gives 500 unit cells. The adequacy of using a 2D FE model was justified in [28].

The loading, constraints and specimen geometry give several symmetries that, without loss of generality, allow the calculation of a reduced part of the specimen. Taking the time-consuming calculations of the half-size specimens into consideration, a 2D finite element model of 5×5 unit cells is used. This makes a square segment containing 25 unit cells with the side length $L = 5$, $\ell = 0.5$ mm. The selection of the reduced model is assured by a comparison of results with a half-size model made in a preliminary calculation that shows a perfect match of the results, as is further elaborated in Subsection 4.2.

The reason for not reducing the model size further to include just a single column is due to the expected narrow region of localised strain that traverses the specimen at an angle to the loading direction. It is expected since it eventually happens for homogeneous materials that are governed by von Mises yield condition and its associated flow rule under plane stress conditions when it is exposed to a uniaxial load. At least as long as the stress does not exceed critical levels for the initiation of voids, cracks or other faults that lead to early failure. Further details regarding the selected square region of 5×5 unit cells are given in Subsection 4.9.

In the present work, a finite element method is used to simulate the uniaxial tension of seven different materials spanning from phase rheological model A to ditto model B. For all materials, 19 fractions of volumetric contents of 0, 23, 27, 30, 35,... 90, 95, 99 and 100% of UFG skeleton were modelled. The 0% and 100% mean pure CG respective pure UFG materials.

Boundary conditions

The 5×5 unit cells square model is subjected to two boundary conditions on each of the four edges. With the notation u and v used for displacements in the x and y directions, the boundary conditions give a constrained displacement $u = 0$ along the left vertical edge at $x = 0$ and incrementally increased displacement $u = \delta$ along the right vertical edge at $x = L$. The upper edge at $y = L$ entertains symmetry boundary conditions, while the lower edge at $y = 0$ is traction-free. All boundaries are free from shear tractions, i.e. $\tau_{xy} = 0$ on all edges. The complete set of boundary conditions is included in Fig. 2.

Finite elements, meshing and method

Figure 2a shows the 5×5 unit cells with the circular inclusions and the applied boundary conditions. Figure 2b shows a typical mesh for a unit cell with 60% of the volume covered by the CG inclusions shown in green. The centre positions of the circular inclusions are the same for all amounts of CG from 1% to 77%, while the radius varies.

Plane stress three-node constant strain elements (CPS3) are used, cf. Abaqus/CAE [34]. The mesh is obtained by a Delaunay type of triangulation algorithm, cf. [35], with a higher element density in the narrow regions of UFG ligaments confined between the CG inclusions. The calculations are performed using a large strain formulation and Cauchy stresses. For plane stress, this means that what is called generalised strain is invoked. This means that the local thickness $h = h(x, y)$ is considered for equilibrium, i.e.

$$\frac{\partial(h\sigma_x)}{\partial x} + \frac{\partial(h\tau_{xy})}{\partial y} = 0 \text{ and } \frac{\partial(h\tau_{xy})}{\partial x} + \frac{\partial(h\sigma_y)}{\partial y} = 0. \quad (6)$$

Further, the application of load is assumed to be sufficiently slow so that the structure remains unaffected by inertia and viscous material behaviour.

The area percentages covered UFG skeleton are the 19 area fractions 0, 23, 27, 30, 35,... 90, 95, 99 and 100%. The remaining area of each is covered by the CG phase. The reason for the gap between fractions 0 to 23% is that the circular inclusions are not permitted to intersect meaning that the largest possible CG fraction is $\pi/4 \approx 78.54\%$. The number of elements in the 5×5 cells ranges from around 120,000 to slightly

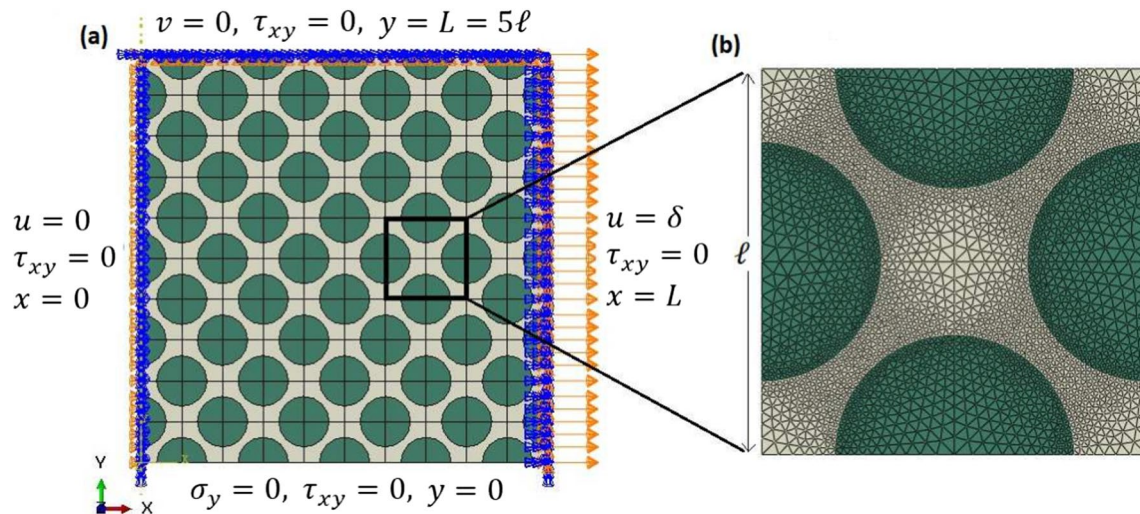**Figure 2** **a** 5×5 unit cells and applied boundary conditions. In this case, 40% of the area is covered by the UFG skeleton, here shown in bright colour. The remaining 60%, shown in dark green, are the CG inclusions. The elongation is controlled by an applied displacement δ of the vertical right-hand side boundary. **b** The mesh is obtained by a Delaunay type of triangulation algorithm, cf. [35].

above 310,000 for the 19 different fractions. The calculations for the smallest and largest inclusions, i.e. the UFG fractions 90 to 99% and 23 to 35%, require the largest element densities to obtain element-independent results before the onset of general structural instability.

Results and discussion

In this section, first preliminary calculations are made to confirm the expected midplane symmetry and to verify the selected 5×5 unit cell including the limited influence of the traction-free surfaces. This is then followed by detailed analyses of the several material models and the span of UFG contents from 0 to 100%.

Dimensional concepts

The problem has a variety of parameters that rely on units of length, such as elongation δ and the specimen dimensions which are $1\times1\times10L^3$ being width, thickness and length. The length L is the single length scale used in this study, which means that as long as all variables given in length units have the same ratio the result will be identical. The selected force unit affects the value of the yield stress, σ_Y, the power law coefficient k, and the modulus of elasticity, meaning that with a force unit, e.g. $\sigma_Y L^2$ all cases have the same ratio of k, E versus the yield stress will give identical results. The remaining parameter, s, cf. Equation (2) is non-dimensional and has to have a fixed value to provide identical results. By using L as the length unit and, $\sigma_Y L^2$ as the force unit, the entire problem becomes non-dimensional and can be applied to any geometry and materials with the same ratios between geometric characteristics measured in length units and between load characteristics measured in units of force. Non-dimensional quantities, e.g. such as the exponent s, have to remain the same.

Qualification of the 5×5 unit cell model

The half specimen geometry and the reduced geometry in Fig. 3 a and b are compiled with coherent boundary conditions showing insignificantly different results of true stress versus strain up to the ultimate load for the two geometries, cf. Figure 3c. The calculated result is expected because of the manifold symmetries that prevail as long as the structures remain stable. The many models that require rather tedious calculations are made possible by the large reduction of CPU time that is achieved with the smaller specimen.
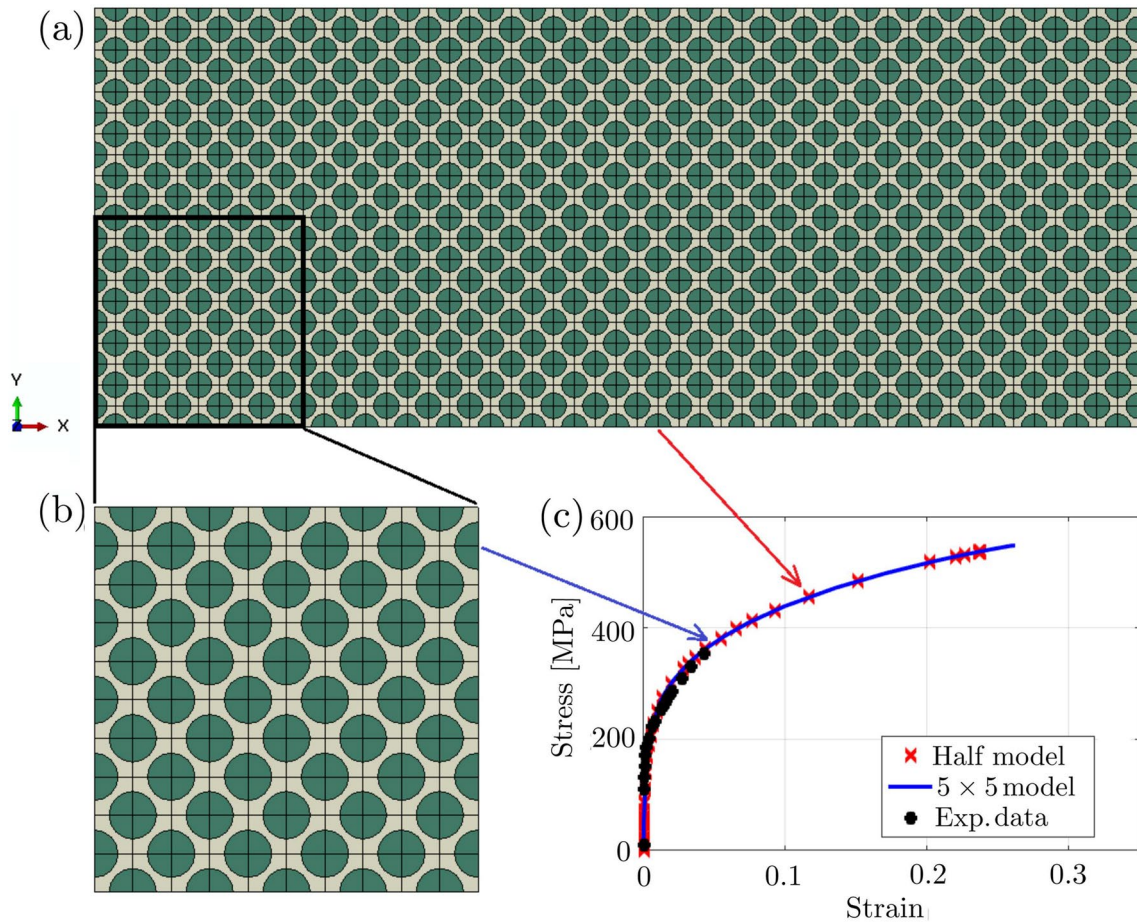
Figure 3 The 2D finite element model for 60% of the volume occupied by the soft coarse grain inclusions in the hard ultrafine grain skeleton. **a** The modelled full width and half length of the frequently used specimen are covered with 10×25 quadratic unit cells each having 4 inclusion halves. **b** The reduced model with 5×5 unit cells. **c** Obtained true stress–strain curves of both geometries along with experimental data from [19].

The symmetry conditions apply to all vertical cuts marked in black through both the geometries. This means that all single columns of half-unit cells could be representative of the entire specimen up to the ultimate load. However, a single column is assumed to be insufficient for two reasons, first, local instability may occur before global instability because of the larger stresses expected at the traction-free surfaces which will reduce the stress along the surface in the neighbouring unit cells. Second, the single-column width limits the possibility of forming a narrow band of localised strain to only a practically vertical one. As a consequence, this would erroneously increase the ultimate load. A quadratic segment would allow faults to propagate down to 45° against the direction of loading. Low angles reduce the load across the failure path

and do therefore not seem plausible. For this study, the quadratic five-column geometry is, therefore, considered to be sufficient.

On the influence of the traction-free boundary

First, a preliminary 10×10 cells column model is computed. The boundary conditions are traction-free surfaces along $0 \leq x \leq 10\ell$ and at both $y = 0$ and 10ℓ. The reason for the larger geometry for this single case is a precaution to check if symmetry prevails and to explore how much of the specimen is affected by the traction-free boundaries. The selected case is for a UFG coverage of 40% at 10% total strain. The phase rheology is described by model B.

Figure 4 with more detailed data in Table 2 shows the reaction forces, F_n, acting on unit cells 1 to 5 with
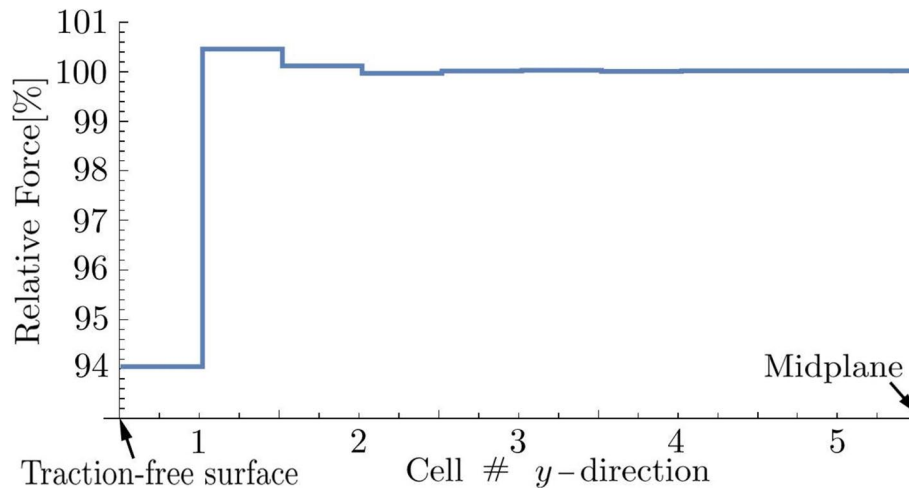
Figure 4 The relative reaction force per half-cell versus y-direction given by the cell number. Forces or equivalently the engineering stresses are normalised with respect to the same at a large distance from the surface. Numbers are 1 starting at the traction-free surface at $y = 0$ and 5 ending at the mid-specimen and the symmetry boundary at $y = L$. The stress distribution is identical across any vertical cut through the 10×5 unit cell part, i.e. at $x/L = 0, 0.05, 0.1, 0.15$.
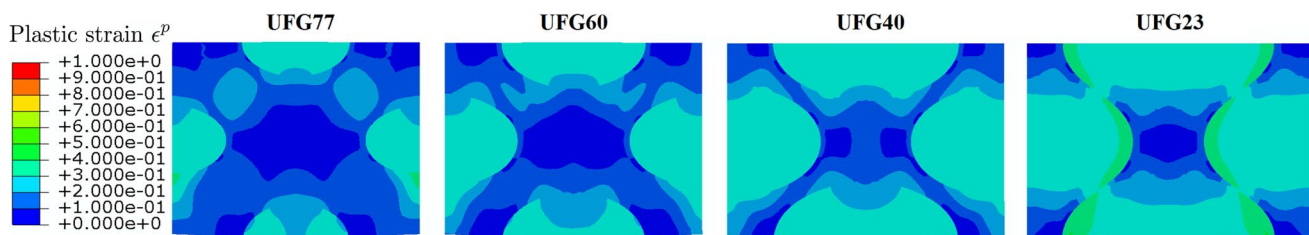

Figure 5 Visualisation of developed typical waviness on the peripheral traction-free surface for volumetric contents 77%, 60%, 40% and 23% UFG. The situation is immediately before the initiation of global instability, i.e. there is no significant difference between the five vertical columns of five unit cells, cf. Figure 3b. The unit cell represents all cells in the bottom row of Fig. 3b. The left and right boundaries remain straight, as is expected from the symmetries across them. Also, the upper boundary is almost straight, indicating that this is practically a symmetry line. This is in line with the observed small differences in reaction forces between all unit cell rows above the lowest half of the unit cells closest to the traction-free boundary, at $y = 0$, cf. Figure 4. The material model parameter $q = 1$, i.e. model B, cf. Figure 1.

Table 2 Reaction forces acting on the 10 half-cell model at $x = 0$ from cell #1 closest to the traction-free surface at $y = 0$ to half-cell #10 closest to the mid-specimen symmetry boundary

Half-cell n	#1	#2	#3	#4	#5	#6	#7-#10
F_n [N]	18991	20286	20217	20187	20196	20199	20196± 1
$F_n/F_{10} - 1$ [%]	−5.97	0.45	0.10	−0.04	0.00	0.01	± 0.00005

a half-cell resolution. The abscissa gives the position of the unit-cell number along the edge at $x = 0$ starting with $n = 1$ for the one closest to $y = 0$ and ending with $n = 5$ for the cell that is closest to the midspecimen boundary at $y = 5\ell$. The relative deviation of

F_n as compared with a deeply embedded cell F_∞, i.e. $(F_n - F_\infty)/F_\infty$ is included in Table 2. For the directions of the Cartesian coordinates x and y and their origin $x = y = 0$, at the lower left corner of the meshes, in Fig. 3a and b.

The reaction forces acting on half-cells #7 to #14 belong to a central region where all cells deviate less than 0.01% from their average. In the middle of the central region, both half-cells #10 and #11 are in equal positions on opposite sides of the symmetry line and are the closest to the mid-specimen symmetry line. They are, therefore, the best representatives of a half-cell at a sufficient distance to be unaffected by the traction-free surface. Therefore half-cell reaction force F_{10} is selected as F_∞.

In addition to the plane stress in the *x-y* plane with absent σ_z, τ_{xz} and τ_{yz}, at the traction-free boundaries where also σ_y, and τ_{xy} vanish we are left with the only possible non-zero stress, σ_x, i.e. a layer close to the surface harbours a uniaxial stress state. The soft inclusions break this layer. The absence of shear stresses τ_{xy} creates a wavy surface. Further, into the material, the waviness would persist, but the shear will be resisted by increasing shear stresses. At some distance from the surface, the deformation is reduced by shear stresses in equilibrium and horizontal unit cell boundaries will become straight and the state will be a so-called generalised plane strain, i.e. absent shear, γ_{xy}, and no total net force in the *y*-direction on each cell boundary, cf. Figure 5.

The deviation from the total reaction force caused by the surfaces would be the total sum of deviations divided by the number of cells across the specimen, as Table 2 readily shows, be around −0.54% for a 10 unit cells wide specimen. The observation supports the assumption that a 5×5 unit cell model is sufficient for predicting results for any specimen with a height of 10 or more unit cells.

Also, a model for a volume of 90% UFG skeleton coverage shows a similar result with insignificant deviations (below 0.5%) between half-unit cells from #3 to #10. However, for very small inclusions, the effect of the free surface may spread to involve more than the two closest half-cells and for sure, in the absence of inclusions the entire specimen is in a plane stress state.

Given the limitations regarding very small inclusions the observations that only the two half-unit cells closest to the traction-free surfaces, deviate from the cells in the interior of the model in any significant way offers a possibility to estimate the stiffness of specimens with widths of both more and fewer unit cells. Thus, a slightly bold suggestion could be that the lowest number, *N*, of full unit cells is at least 3. It seems reasonable that the limitations and advantages apply also to non-symmetric cases. For a symmetric case, the total reaction force, $\mathcal{F}$, for *N* full unit cells, at any given elongation prior to strain localisation, would simply be calculated as follows:

$$\mathcal{F} = \sum_{i=1}^{N} F_i = 2(F_1 + F_2) + (N-4)F_\infty, \tag{7}$$

where *i* represents the unit cell numbers, counted across the specimen from one of the traction-free boundaries. The forces F_1, F_2 and F_∞ may be obtained from numerical results for any specimen with $N \geq 3$.

Tensile properties

Seven phase rheological pairs and for each pair nineteen different composites with different amounts of the UFG content, i.e. altogether 133 models are executed. The material properties are based on phase rheological models A and B and intermediate materials having scaled phase rheological parameters *k* and σ_Y that is given by *q* as is described in Subsection 2.1.

The variation of the amount of UFG phase is based on the different inclusion radii giving 0, 23, 27, 30, 35,... 90, 95, 99 and 100% of UFG. In addition, calculations for pure ultrafine grain and for pure coarse grain are performed.

Figure 6 shows the total reaction force versus the original cross section of 1 mm², i.e., the engineering stress for rheological model A and selected UFG contents. The loading process is stable as long as the incrementally increasing elongation requires an increasing load due to the strain hardening of both materials. The simultaneous reduction of the cross-sectional area counteracts the increase of the load. If no other processes such as fracture, initiation of voids and void growth, or other failure mechanisms occur then the decreasing strain hardening rates inevitably lead to loss of load-carrying capacity. It happens when the effect of the cross-sectional reduction rate exceeds the effect of the strain hardening rate, according to Considére's condition.

At this point, the elongation is limited to the straining across a single narrow band traversing the specimen. The rest of the specimen will predominantly, experience only elastic unloading. The initiation of cracks or voids is not anticipated. Further, the minimum width of the band of localised strain is constrained by the size of the elements which limits the rate of load decrease versus elongation, i.e. what is the dashed part of the curves in Fig. 6. In the real

Figure 6 Engineering stress $\sigma = \Sigma F_i / L^2$ versus elongation δ/L for material model A, i.e. $q = 0$, and different UFG volumetric fractions, cf. Figure 1. The solid curves mark stable loading. The transition to the dashed curves marks the load maximum at the onset of global strain concentration (i.e. ultimate strength), and structural instability (i.e. uniform tensile strength).
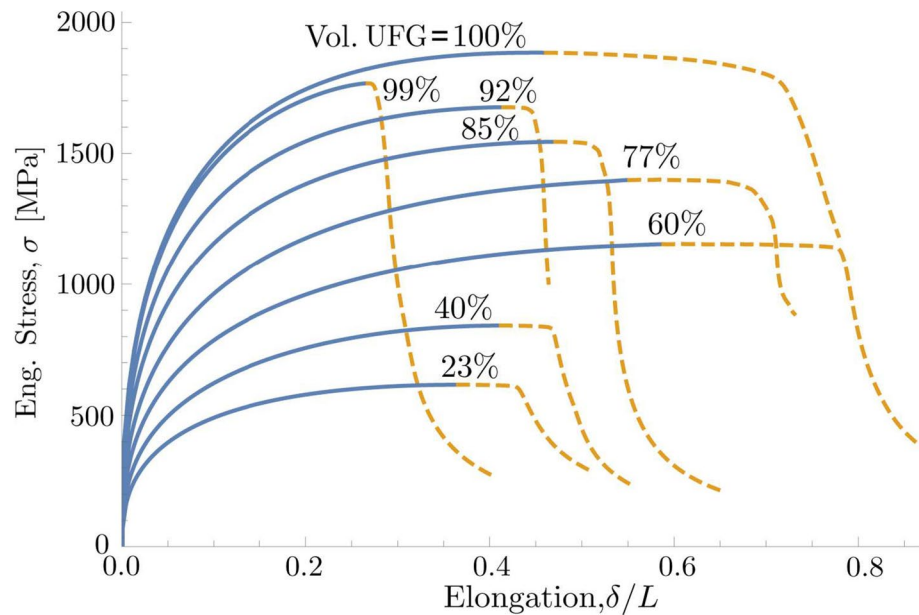
world, the thickness of the specimen would affect the width of the region of localised strain, i.e. the dashed part of the curves.

Things become dependent on the length of the two unloading parts, which is almost the entire specimen length. While the width of the band of localised strain becomes as thin as the elements allow. During the process, there is a flux of released energy from the elastically unloading parts to the narrow energy-consuming band of localised strain. The energy consumed during the formation of the narrow band of localised strain is dependent on the element size. Because of this, the primary focus of the present study is on the structural behaviour until the ultimate load is reached.

The dependencies of the ultimate tensile stress and the uniform elongation on the UFG skeleton fraction are plotted in Fig. 7a and b, respectively, for seven material models (q =0, 0.1, 0.25, 0.5, 0.75, 0.9 and 1) for each of 19 different volumetric percentages of the UFG phase. The markers in the figure show the results of the 133 calculated combinations of phase rheology and geometric models.

As Fig. 7a shows, the ultimate load-carrying capacity increases monotonically and nearly proportionally with increasing UFG content, which agrees well with the results presented in Fig.6. It is also interesting to note that the increase of strength is very modest when the HS models have low strain hardening, i.e. at high q values. However, the higher

the strain hardening of the phases the stronger the effect of increasing UFG fraction with a sharp increase between 99% and 100% UFG phase.

When it comes to the dependence of elongation (ductility) on the UFG fraction, see Fig. 7b, the trend is opposite. The largest linear drop down to a minimum ductility at 100% UFG is found in the HS material with the lowest strain hardening, i.e. q=1. Very interestingly, the dependence of elongation on UFG fraction becomes non-monotonic for the HS models having substantial strain hardening, q >0.9. Three characteristic UFG fractions can be distinguished for such phase rheologies including two local minima and one maximum as follows:

(I)   In the range of approximately 30% UFG fraction, the first minimum can be found beyond which the increase of UFG phase leads to an increase in ductility.

(II)   At approximately 60% UFG fraction, the increase of ductility reaches a local maximum and starts decreasing with a further increase in UFG fraction. The discussion of this maximum is elaborated in subsection 4.6.

(III) At approximately 98% UFG fraction, a second local minimum in ductility can be found.

It is also important to notice that the level of ductility at 40% UFG is higher than at 100% CG counterpart for HS phase rheologies having the highest strain hardening,
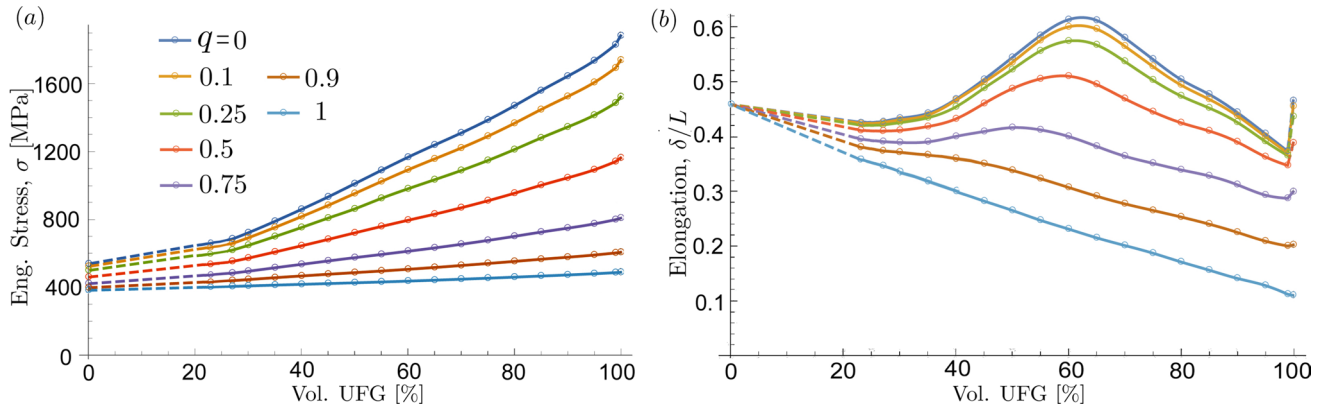
Figure 7 **a** The ultimate stress $\sigma_m = F_m/L^2$ and **b** the respective uniform elongation δ/L summarised from stress–strain curves such as shown in Fig. 6, for phase rheology models A ($q = 0$) and B ($q = 1$) and five intermediate rheological models, cf. Figures 1 and 2. The results are plotted versus the volumetric fraction of the UFG skeleton encapsulating the CG inclusions.

i.e. when $q \geq 0.25$. The effects of characteristic UFG fraction (III) are discussed in detail in subsection 4.5, while those for UFG fractions (I) and (II) in 4.6. In summary, the trends presented in Fig. 7 are consistent with our prior experimental results, [13, 14, 36]. At the same time, they go beyond the previous findings into the range of higher UFG fractions and suggest possibilities for further optimisation of HS materials performance.

Effects of infinitesimal inclusion size compared with pure UFG material.

Figure 7b shows that all HS models suffer from similar elongation drops (local minima) when a very small fraction of CGs remains in the microstructure as infinitesimally small inclusions at 99% UFG. The largest increase is obtained for HS phase rheology model A, i.e. for q=1. It is also interesting to note that the dependence of ductility characteristics such as uniform elongation on UFG fraction is non-monotonic.

The drop is caused by the small inclusions and the stress concentration that each one of them causes. When the inclusions are as small and sparse as they are for only 1% coverage, the average stress becomes insignificantly affected by the present inclusion. On the other hand, the largest local stress remains constant and depends only on the shape and the materials differences and not the size of the inclusion. Even a single inclusion would produce the same stress concentration provided that it is small. It would not affect the average stress but with the same local

stress concentration it produces the same role as a source of localised strain and as a starting point of a propagating fault. Once the fault extends outside the vicinity of the traction-free surface the fault will rapidly traverse the specimen and cause global instability. A condition is of course the element mesh is sufficiently refined in parallel with the decreasing inclusion sizes to allow the formation of the narrow band of localised high strains. The large difference between extremely small inclusions is that the large local stress creates conditions for the initiation and growth of a fault that traverses the specimen. The complete absence of inclusions delays the event and results in a significantly larger ultimate strain and discontinuous behaviour as compared with any infinitesimal inclusions.

The largest elongation at the ultimate load.

Figure 8 shows a summary of the skeleton volume fraction that gives the peak elongation for each model parameter q cf. Equation 5. For $q \gtrsim 0.6$ the local maximum is exceeded by the pure CG material which provides a larger elongation at the ultimate load than any of the HS material models. However, the pure CG material has a considerably lower stress. For material models with $q \geq 0.88$, a local maximum elongation does not appear.

In addition to this, it is interesting to note that the experimental result, i.e. a local maximum elongation obtained for 40% volumetric percentage UFG, reported in [14] is here obtained for a material with

Figure 8 The UFG skeleton volume fraction gives the peak elongation for each HS model parameter q mix of HS model A ($q = 1$) and B ($q = 0$). For $q \gtrsim 0.6$, the local maximum is surpassed by the pure CG material. For the largest possible cylindrical inclusions, the maximum is obtained for the material model given by $q \approx 0.91$.
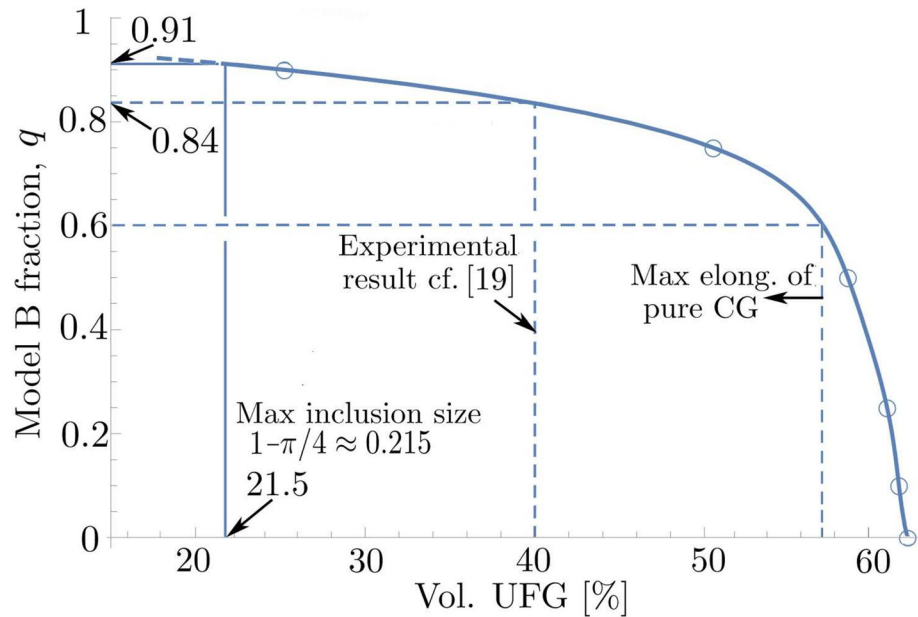
$q \approx 0.84$ which is fairly close to HS rheological model B.

When these results are considered in a broader context of heterogeneous materials, e.g. [6], the direct translation is not straightforward. The highest level of similarity can be observed in the dependence of strength characteristics on UFG phase fraction. However, the dependence of ductility characteristics on the same varies significantly depending on heterogeneity type. Compared to the gradient and lamellae-type heterogeneities, HS materials demonstrate significantly more distinct non-monotonic dependence, which also increases magnitude with the increase of strain hardening capacity in each phase. At the same time, dual-phase steels and multimodal structure materials are more similar to HS, while the latter typically demonstrate a more regular pattern of heterogeneity distributions and therefore easier to control.

Normal and principal stresses in the interior of the specimen

The traction-free surfaces only affect the unit cell row that is closest to the surfaces as is described in Subsection 4.3. The variation is less than 0.5% in all other unit cells. Along each row, all cells have the same result with no variation at all before strain localisation is initiated. Therefore, the result along $0 \leq x \leq \ell$ at $y = 5\ell$, shown in Fig. 9, surprisingly well represents all unit

cell boundaries at $y = \ell, 2\ell, ..., 8\ell$ and 9ℓ all cells apart from the traction-free boundaries at $y = 0$ and $y = 10\ell$. Three volumetric percentages of 23%, 40% and 77% UFG phase are selected, which encompasses a reasonable range of useful materials.

The symmetry across the x-axis at $y = 5\ell$ and the traction-free surfaces at $y = 0$ and $y = 10\ell$ require that the shear stresses vanish, i.e. $\tau_{xy} = 0$. Therefore, the normal stresses σ_x, σ_y and σ_z are principal stresses. As is observed in Fig. 9 σ_y is at all locations with ample margins, lower than σ_x, which means that $\sigma_x = \sigma_1$ is everywhere along $y = 5\ell$ the largest principal stress, whereas the second and third largest principal stresses σ_2 and σ_3 shift between σ_y and σ_z depending on whether σ_y is tension or compression. The observation also suggests that if a crack is initiated it will initially be perpendicular to the tensile x-direction.

The stress distribution for different columns of unit cells may vary because of mesh differences. The differences may escalate when instability is imminent. With an exact solution, all differences should be absent. Obviously, along the midplane $y = 5\ell$ the stress state is practically identical along each unit cell. The original suggestion $y = \ell$, i.e. on the top of the unit cell at the traction-free surface, would be the best if it turns out to be reasonably close to $y = 5\ell$. If the differences are fairly small, it is reasonable to assume that all cells in x from -2.5ℓ to 2.5ℓ and y from 2ℓ to 8ℓ, have the same stress states. This
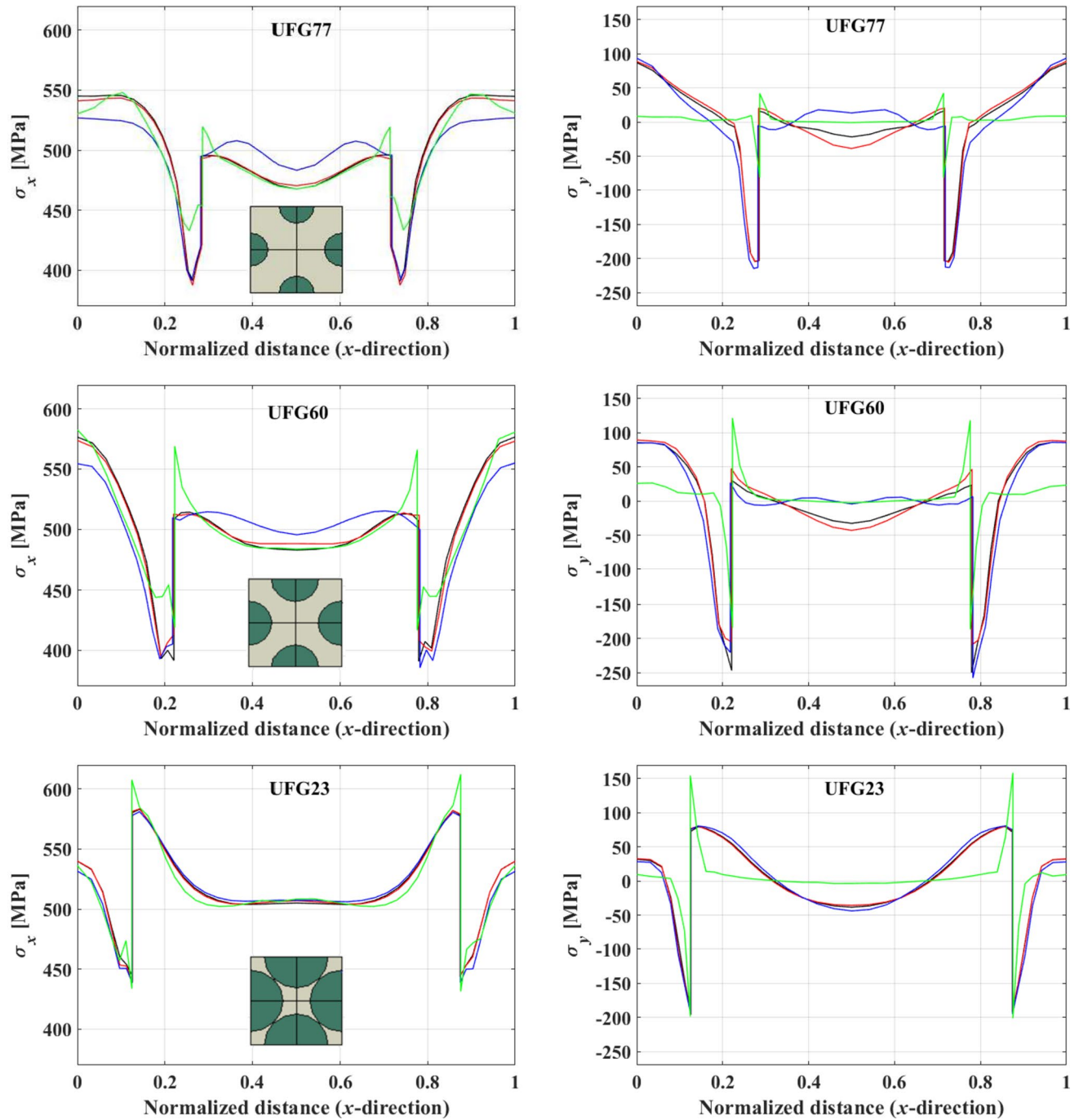
Figure 9 Stresses across a unit cell along the traction-free surface at $y = 0$ (green), and in the interior at $y = 0.5\ell$ (blue), $y = \ell$ (red), and along the mid surface at $y = 5\ell$ (black). The selected rheological model is for $q = \ell$, i.e., according to model B. While the unit cells assume almost identical results across the specimen in at least the region $\ell \leq y \leq 9\ell$, the shear stress, τ_{xy}, is insignificant. Adding to this, the plane stress conditions imply that

σ_x, σ_y and σ_z become the principal stresses. Further, σ_x is readily observed to be the largest principal stress. Of the shear stresses acting on the xz and the yz planes, i.e. $\tau_{xz} = \sigma_x/2$ and $\tau_{yz} = \sigma_y/2$, τ_{xz} is the largest and constitutes a potential risk for onset of localised shearing and thickness reduction, which is the only failure mechanism in the present paper.
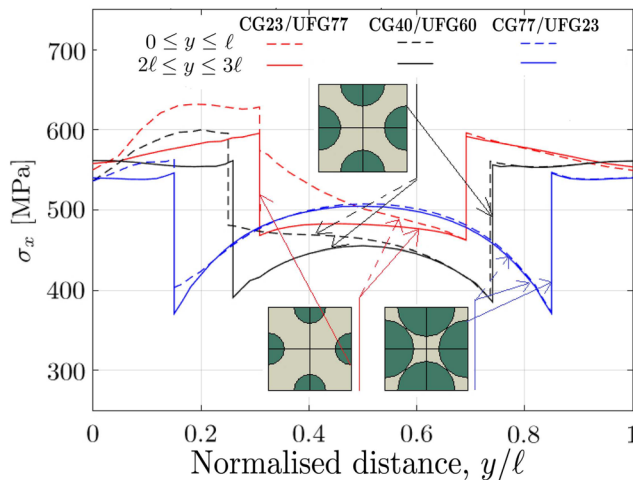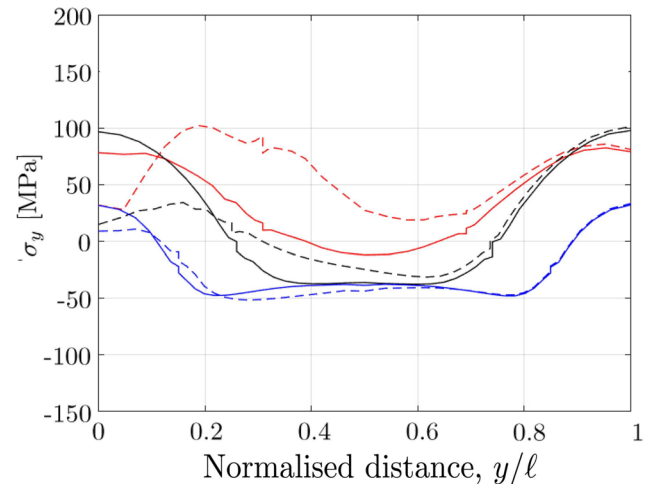
Figure 10 $\sigma_x = \sigma_1$, and σ_y, along the edge at $x = 5\ell$ and $0 \leq y \leq \ell$. It is observed that the result from $y \geq 0.5\ell$ is close to that in the interior of the specimen for CG40/UFG60 and CG77/UFG23. The interior is here represented by the solid curve, i.e.

for $2\ell \leq y \leq 3\ell$. For CG23/UFG77 the same would be from the upper edge of the inclusion. The stress σ_x is, as observed always to be the largest stress, which makes it the largest principal stress, i.e. $\sigma_x = \sigma_1$, whereas σ_y and $\sigma_z = 0$ switch between σ_2 and σ_3.

is already suggested by the right side of the curves in Fig. 10. Also, Table 2 suggests that the error is 0.1% which is considered to be small compared to the numerically introduced errors at a normal FEM analysis.

The stress of interest displayed in Fig. 9 is the largest principal stress. It is known to initiate cracks in brittle materials. Figure 9a shows that $\sigma_x = \sigma_1$ reaches around 550 MPa in the UFG skeleton and around 500 MPa in the CG inclusion for the 77% UFG content. The model with 60% UFG has a marginally larger stress close to the middle of the UFG skeleton and significantly large in the CG inclusion close to the CG/UFG interface. For the largest inclusion having 23% UFG content, the stress peak in the UFG skeleton is slightly less, i.e. around 540 MPa but considerably larger in the CG inclusions with a peak at 610 MPa at the traction-free surface, while it reaches 580 MPa in the interior of the specimen. The peak principal stress must of course be judged against the brittleness and sensitivity of each material. Such back / forward stress ratios at the interface of UFG skeleton / CG inclusions, respectively, are in a very good agreement with our earlier experimental [31], analytical [30] and FE modelling [28] studies.

Figure 10 shows the stresses σ_x and σ_y along $x = 5\ell$ for $0 \leq y \leq \ell$ and $2\ell \leq y \leq 3\ell$. Also here at $x = 5\ell$ the

shear stresses vanish because of the symmetry across the y-axis, which makes σ_x and σ_y principal stresses. The result is representative of all unit cell boundaries in this case for $x/\ell = 0, 1, 2, 3, 4$ and 5, since all unit cells in each row have identical states until the initiation of strain localisation. The variation of stress is periodic along the y-axis except for the unit cell closest to the traction-free surface, which confirms the results from Subsection 4.3

Figure 10a shows that $\sigma_x = \sigma_1$. In the unit cell closest to the traction-free surface at $0 \leq y \leq 0.1$ mm, for the 77% UFG content, the stress reaches around 630 MPa in the UFG skeleton and around 580 MPa in the CG inclusion. In the same unit cell, for the inclusion having 60% UFG content the stress peak in the UFG skeleton is around 600 MPa and slightly less in the CG inclusions with a peak at around 490 MPa. Finally, the 23% UFG content material has a principal stress peak in the UFG skeleton is around 560 MPa and in the CG inclusions a peak at around 500 MPa. It is interesting to note that the latter occurs in the middle of the inclusion as opposed to the smaller inclusions where the maximum is at the UFG/CG interface.

The result for the remaining unit cells the stresses are slightly lower for both 23%, 60% and 77% UFG contents. The drop of the principal stress is around
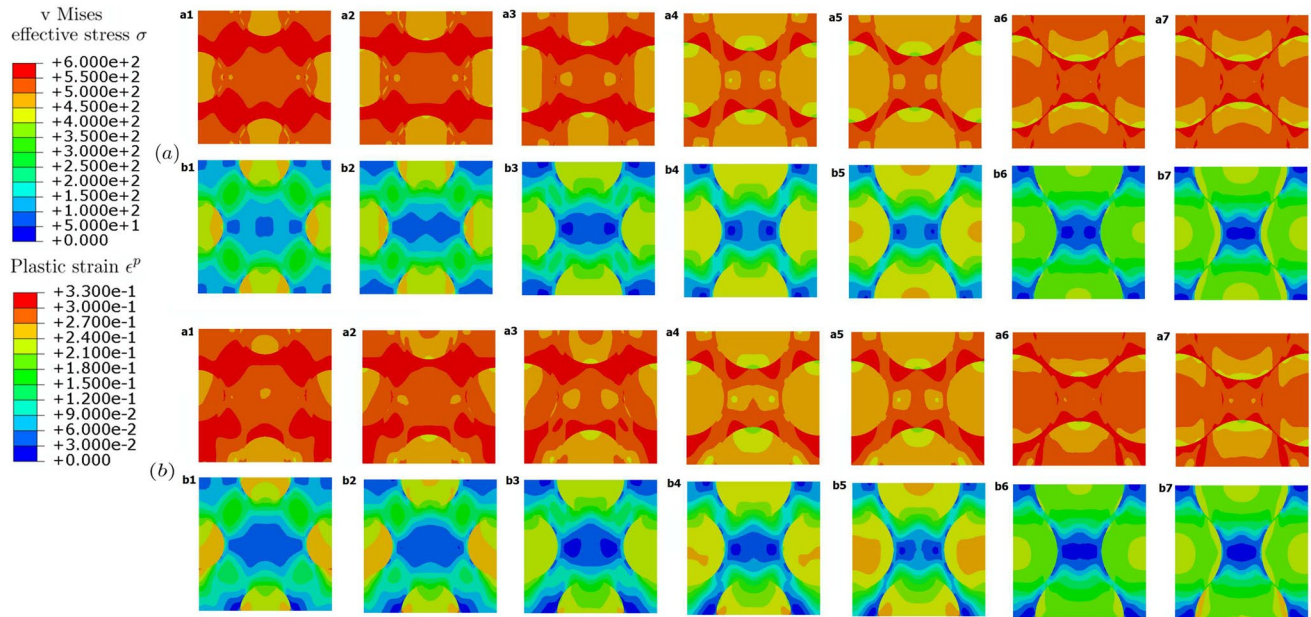
Figure 11 Contour plots a1 to a7 are von Mises effective stresses σ_e and b1 to b7 are the effective plastic strains ϵ_e^p. The first and second rows, marked **a**, are for the upper cells closest to the specimen midplane and the third and fourth rows, marked **b**, are the cells closest to the traction-free surface. The numbering of a1, b1, a2, b2, etc. refers to the UFG skeleton of volumetric fractions 77, 70, 60,...30 and 23%.

5%, 7%, 3% in the UFG skeleton and 18%, 6%, 2% in the CG inclusion for volumetric percentages UFG of 77%, 60% and 23% respectively.

It is interesting to note that whatever stress-controlled failure, e.g. cross-sectional necking, fatigue, crack initiation and fracture, is likely to start close to the traction-free surface. The strain localisation followed by necking is observed to initiate at the traction-free surface, cf. Subsections 4.8 and 4.9.

Contour plots of equivalent stress and plastic strain distributions.

The results for different fractions of the UFG phase for a load immediately before the ultimate load are shown in Fig. 11. Contour plots of von Mises true stress are marked a1 to a7, and plots marked b1 to b7, show the equivalent plastic strains associated with von Mises yield condition for a unit cell closest to the midplane of the specimen. Figure 11b shows the same as a, but for one of the unit cells closest to the traction-free boundary.

The same colour scale is used for all seven fractions for comparison reasons. Both the midplane cell (a)

and the traction-free boundary cell (b) in the 5×5 cell model show that the largest stresses are concentrated in the UFG regions. This is a natural consequence of the geometrical reality that the UFG phase skeleton is continuous between the left and right ends of the specimen and that it has a much higher strength. The UFG phase skeleton carries a proportionally larger part of the load. As long as both are elastic they have the same stress due to their identical elastic properties. When plastic deformation sets in and the material remains continuous the UFG material as being the hardest, will take the largest stress. For a more comprehensive discussion on the continued plastic deformation, cf. [28].

Formation of a specimen-traversing region of localised strain

A required condition for the formation of a traversing region of localised strain, i.e. a so-called neck, is a line-shaped region that only has strain increase across and no strain increase in the direction of it. Consider a thin homogeneous body that is exposed to uniaxial
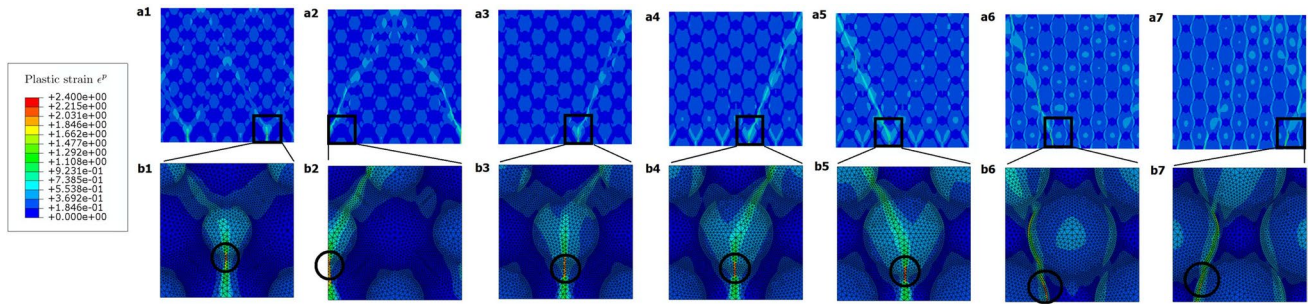
Figure 12 Contour plots for equivalent plastic strain for different UFG fractions at the early start of element distortion for 5×5 unit cells **a1**–**a7** and enlarged parts **b1**–**b7**. The numbers 1-7 indicate the UFG skeleton of volumetric fractions 77, 70, 60,...30 and 23%, respectively.

Table 3 The orientation of the necking region traversing the specimen for different UFG contents as measured in the undeformed representation of Fig. 12. The measured angle θ_n^* is converted to the true physical angle θ_n via Eq. 11

% UFG	$\epsilon_x = u/\ell$	$\epsilon_y = v/\ell$	θ_n^*	θ_n
23	0.670	0.145	72°	60°
30	0.700	0.291	66°	55°
40	0.663	0.293	65°	54°
50	0.576	0.265	64°	54°
60	0.470	0.219	66°	55°
70	0.451	0.223	64°	53°
77	0.352	0.167	64°	53°

stress σ_o. A straight necking line forming at an angle θ_n to the direction of the tension, according to rules for 2D transformation of coordinate directions, becomes

$$\sigma_n = \sigma_o \cos^2 \theta_n \text{ and } \sigma_t = \sigma_o \cos^2(\pi/2 + \theta_n) = \sigma_o \sin^2 \theta_n. \tag{8}$$

The von Mises plastic strain increments are proportional to the deviatoric stress. Thus, using Eq. 8 the strain increment, $\mathrm{d}\epsilon_n$, along the necking line becomes

$$\mathrm{d}\epsilon_n = \mathrm{d}\lambda \left(\sigma_n - \frac{1}{3}(\sigma_t + \sigma_n) \right) = \mathrm{d}\lambda\, \sigma_o \left(\cos^2 \theta_n - \frac{1}{3} \right), \tag{9}$$

which readily gives that $\mathrm{d}\epsilon_n = 0$ when

$$|\theta_n| = \arccos\left(1/\sqrt{3} \right) \approx 54.7° \tag{10}$$

Figure 12 shows contour plots of the equivalent plastic strain for the 5×5 cells model closely before initiation of global structural instability for rheologic model B. The figure shows the spots of the largest plastic deformation encircled by black circles. The distortion of elements starts in the UFG areas that have large and moderate percentages of UFG phases (see Fig. 12b1-b5).

The necking in these models initiates in UFG areas close to the interface between the UFG-CG phases interface. The subsequent propagation proceeds in the
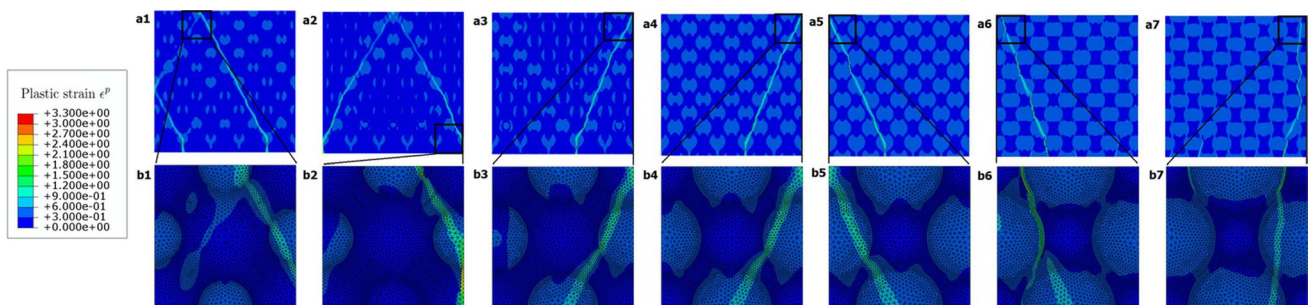

Figure 13 Contour plots for the progression of the localised equivalent plastic strain of the 5×5 cells **a1**–**a7** and enlarged parts **b1**–**b7**. As in Fig. 12, the numbers 1-7 represent the UFG volumetric fractions 77, 70, 60,...30 and 23%.

CG areas along a direction in the range from 53°to 60° against the tensile direction (see Fig. 12 a1–a7). Due to the limited UFG fraction between the adjacent CG areas in 30% and 23% of UFG areas, the neck starts at the adjacent area between CG areas and UFG areas, then it also propagates locally with almost 45°, after a short almost vertical growth (see Fig. 12b6 and b7).

The plots in Fig. 12 are presented in undeformed states, which gives an apparently larger slope than the true one.

Table 3 shows the apparent angle θ_n^* as given in Fig. 12 is translated to the real angle by using

$$\theta_n = \arctan \frac{\sin(\theta_n^*)(1 + \epsilon_y)}{\cos(\theta_n^*)(1 + \epsilon_x)}. \tag{11}$$

Figure 13 shows contour plots of the obtained von Mises equivalent plastic strains for the different fractions after distortion of elements, for 5×5 cells a1–a7 and enlarged one cell with meshed elements b1–b7. The scale has been fixed for comparison reasons both as regards the different fractions and the result in Fig. 12. The results show that almost all fraction models have the same necking pattern.

Conclusions

In the interest of understanding the effect of the UFG fraction on the mechanical behaviour of HS materials, seven rheological pairs with different yield stresses and hardening rates were used for 19 different fractions of UFG phases embedding uniformly distributed CG inclusions into a skeletal network. This makes 133 cases, together with a few special cases, analysed for monotonically increasing elongation up to and slightly beyond the maximum load and strain localisation. Based on the reported results, the following conclusions are made:

- The largest elongation is obtained for the rheological model A, i.e. the HS material model with the highest hardening rates. The optimal fraction of the UFG phase providing maximum uniform elongation is close to 60%. At the same time, the ductility of HS material may supersede that of CG counterpart already at 40% UFG.
- The presence of even the smallest inclusions gives a severe drop in maximum load as compared with the pure UFG material and a drastic drop of elongation at maximum load. This is expected while the local stress distribution, on the level of the inclusion, becomes finite and independent of the inclusion size for infinitesimally small CG inclusions. For the UFG phases with the highest hardening rates, the drop in elongation at maximum load is up to 20%.
- Necking traversing the specimen occurs at 53° to 55° to the loading direction for all CG inclusion volumes apart from the largest, i.e. 77% vol. CG that forms a necking region 60° to the loading direction. The observation is surprisingly close to the theoretical 54.7° for homogeneous materials that comply with the von Mises yield criterion and flow rule.
- The stress and strain states develop identically in all columns of unit cells before the maximum load is reached. Within each column, the state of the individual unit cells is almost identical within a difference in load of less than 0.1%, except for the unit cell closest to the traction-free boundary. The very limited influence of the traction-free boundary indicates that a specimen model of 1×2 unit cells should be sufficient for the prediction of loads prior to strain localisation for any larger specimen. The result is readily given by a simple algebraic relation. For specimens with many unit cells, a single unit cell should be sufficient.

Data availibility statement

Numerical data are available on request.

Declarations

Conflict of interest   Neither of the authors has any conflict of interest.

Consent to publication   All authors consent to publication.

References

[1] Edalati K et al (2022) Nanomaterials by severe plastic deformation: review of historical developments and recent advances. Mater Res Lett 10:163–256. https://doi.org/10.1080/21663831.2022.2029779

[2] Estrin Y, Vinogradov A (2013) Extreme grain refinement by severe plastic deformation: a wealth of challenging science. Acta Mater 61:782–817. https://doi.org/10.1016/j.actamat.2012.10.038

[3] Gleiter H (1989) Nanocrystalline materials. Prog Mater Sci 33:223–315. https://doi.org/10.1016/0079-6425(89)90001-7

[4] Meyers MA, Mishra A, Benson DJ (2006) Mechanical properties of nanocrystalline materials. Prog Mater Sci 51:427–556. https://doi.org/10.1016/j.pmatsci.2005.08.003

[5] Ovid'ko IA, Valiev RZ, Zhu YT (2018) Review on superior strength and enhanced ductility of metallic nanomaterials. Prog Mater Sci 94:462–540. https://doi.org/10.1016/j.pmatsci.2018.02.002

[6] Zhu Y et al (2021) Heterostructured materials: superior properties from hetero-zone interaction. Mater Res Lett 9:1–31. https://doi.org/10.1080/21663831.2020.1796836

[7] Wang Y, Chen M, Zhou F, Ma E (2002) High tensile ductility in a nanostructured metal. Nature 419:912–915. https://doi.org/10.1038/nature01133

[8] Ameyama K et al (2022) Harmonic structure, a promising microstructure design. Mater Res Lett 10:440–471. https://doi.org/10.1080/21663831.2022.2057203

[9] Orlov D, Ameyama K (2020) Critical assessment 37: harmonic-structure materials - idea, status and perspectives. Mater Sci Technol 36:517–526. https://doi.org/10.1080/02670836.2020.1719306

[10] Orlov D, Fujiwara H, Ameyama K (2013) Obtaining copper with harmonic structure for the optimal balance of structure-performance relationship. Mater Trans 54:1549–1553. https://doi.org/10.2320/matertrans.MH201320

[11] Ameyama K, Fujiwara H (2012) Creation of harmonic structure materials with outstanding mechanical properties. Mater Sci Forum 706–709:9–16. https://doi.org/10.4028/www.scientific.net/MSF.706-709.9

[12] Vajpai SK, Ota M, Zhang Z, Ameyama K (2016) Three-dimensionally gradient harmonic structure design: an integrated approach for high performance structural materials. Mater Res Lett 4:191–197. https://doi.org/10.1080/21663831.2016.1218965

[13] Zhang Z, Orlov D, Vajpai SK, Tong B, Ameyama K (2015) Importance of bimodal structure topology in the control of mechanical properties of a stainless steel. Adv Eng Mater 17:791–795. https://doi.org/10.1002/adem.201400358

[14] Zhang Z, Vajpai SK, Orlov D, Ameyama K (2014) Improvement of mechanical properties in SUS304L steel through the control of bimodal microstructure characteristics. Mater Sci Eng, A 598:106–113. https://doi.org/10.1016/j.msea.2014.01.023

[15] Vajpai SK et al (2015) The development of high performance Ti-6Al-4V alloy via a unique microstructural design with bimodal grain size distribution. Metall Mater Trans A 46:903–914. https://doi.org/10.1007/s11661-014-2649-7

[16] Kikuchi S, Takemura K, Hayami Y, Ueno A, Ameyama K (2015) Evaluation of the fatigue properties of Ti-6Al-4V alloy with harmonic structure in 4-points bending. J Soc Mater Sci, Japan 64:880–886. https://doi.org/10.2472/jsms.64.880

[17] Dirras G, Ota M, Tingaud D, Ameyama K, Sekiguchi T (2015) Microstructure evolution during direct impact loading of commercial purity of titanium with harmonic structure design. Matériaux Tech 103:311. https://doi.org/10.1051/ma]ech/2015031

[18] Nagata M, Horikawa N, Kawabata M, Ameyama K (2019) Effects of microstructure on mechanical properties of harmonic structure designed pure Ni. Mater Trans 60:1914–1920. https://doi.org/10.2320/matertrans.MT-M2019145

[19] Orlov D, Zhou J, Hall S, Ota-Kawabata M, Ameyama K (2019) Advantages of architectured harmonic structure in structural performance. IOP Conf Series: Mater Sci Eng 580:265–272. https://doi.org/10.1088/1757-899x/580/1/012019

[20] Latypov MI, Alexandrov IV, Beygelzimer YE, Lee S, Kim HS (2012) Finite element analysis of plastic deformation in twist extrusion. Comput Mater Sci 60:194–200

[21] Kim JH, Lee MG, Kang JH, Oh CS, Barlat F (2017) Crystal plasticity finite element analysis of ferritic stainless steel for sheet formability prediction. Int J Plast 93:26–45

[22] Lim H, Bong HJ, Chen SR, Rodgers TM, Babaile CC, Lane JMD (2018) Developing anisotropic yield models of polycrystalline tantalum using crystal plasticity finite element simulations. Mater Sci Eng, A 730:50–56

[23] Kim JG, Latypov M, Pardis N, Beygelzimer YE, Kim HS (2015) Finite element analysis of the plastic deformation in tandem process of simple shear extrusion and twist extrusion. Mater Design 83:858–865

[24] Vinogradov A, Estrin Y (2018) Analytical and numerical approaches to modelling severe plastic deformation. Prog Mater Sci 95:172–242

[25] Moradpour M, Khodabakhshi F, Mohebpour SR, Eskandari H, Haghshenas M (2019) Finite element modeling and experimental validation of CGP classical and new cross routes for severe plastic deformation of an Al-Mg alloy. J Manuf Process 37:348–361

[26] Shimokawa T, Hasegawa T, Kiyota K, Niiyama T, Ameyama K (2022) Heterogeneous evolution of lattice defects leading to high strength and high ductility in harmonic structure materials through atomic and dislocation simulations. Acta Mater 226(117679):1–15

[27] Wang X, Cazes FB, Li J, Hocini A, Ameyama K, Dirras G (2019) A 3D crystal plasticity model of monotonic and cyclic simple shear deformation for commercial-purity polycrystalline Ti with a harmonic structure. Mech Mater 128:117–128. https://doi.org/10.1016/j.mechmat.2018.10.006

[28] Shokry A, Ahadi A, Ståhle P, Orlov D (2021) Improvement of structural efficiency in metals by the control of topological arrangements in ultrafine and coarse grains. Sci Rep 11(1):1–14

[29] Nickel – Element information, properties and uses, http://www.rsc.org, Royal Society of Chemistry. Read July 29 (2022)

[30] Orlov D, Kulagin R, Beygelzimer Y (2020) Strain partitioning and back-stress evaluation in harmonic-structure materials. Mater Lett 275:128126. https://doi.org/10.1016/j.matlet.2020.128126

[31] Sjögren-Levin E et al (2023) Stress partitioning in harmonic structure materials at the early stages of tensile loading studied in situ by synchrotron X-ray diffraction. Scripta Materialia 226:115–186

[32] Beigelzimer JAE, Efros BM, Varyukhin VN, Khokhlov AV (1994) A continuum model of a structurally inhomogeneous porous body and its application for the study of stability and viscous fracture of materials deformed under pressure. Eng Fract Mech 48(5):629–640

[33] Beygelzimer Y (2005) Grain refinement versus voids accumulation during severe plastic deformations of polycrystals: mathematical simulation. Mech Mater 37:753–767. https://doi.org/10.1016/j.mechmat.2004.07.006

[34] Smith M (2009) ABAQUS/Standard User's Manual vers. 6.13, Dassault Systèmes

[35] Kolmogorov AN, Delaunay BN (1969) Mathematics: Its Content, Methods and Meaning, chapter Analytic Geometry. MIT Press, Boston, USA

[36] Sawangrat C, Kato S, Orlov D, Ameyama K (2014) Harmonic-structured copper: performance and proof of fabrication concept based on severe plastic deformation of powders. J Mater Sci 49:6579–6585